Supplementary Information for

Realizing ampere-level CO_2 electrolysis at low-voltage over woven network of silverene nanobelts with ultrahigh aspect rations via paired with formaldehyde oxidation

Min Zhang[a], Xinyu Wang[b], Junjie Ding[a], Chaogang Ban[a], Yajie Feng[a], Chaohe Xu* [c,d], Xiaoyuan Zhou*[a,c,e,f]

[a] College of Physics and Center of Quantum Materials and Devices, Chongqing University, Chongqing 401331, China
E-mail: xiaoyuan2013@cqu.edu.cn.
[b] Hefei National Research Center for Physical Sciences at the Microscale, School of Chemistry and Materials Science, University of Science and Technology of China, Hefei, Anhui 230026, China
[c] National Engineering Research Center for Magnesium Alloys, Chongqing University, Chongqing 400044, China
E-mail: xche@cqu.edu.cn.
[d] College of Aerospace Engineering, Chongqing University, Chongqing 400044, China
[e] Institute of NEW Energy Storage Materials and Equipment, Chongqing 401135, China
[f] State Key Laboratory of Coal Mine Disaster Dynamics and Control, Chongqing University, Chongqing 400044, China

1. Experimental details

1.1 Chemicals

Silver nitrate ($AgNO_3$), ammonium metavanadate (NH_4VO_3), Acetonitrile (CH_3CN), sodium hydroxide (NaOH), potassium hydroxide (KOH), cesium hydroxide hydrate ($CsOH·H_2O$), formaldehyde (40%, HCHO), and ethanol were obtained from Sinopharm Chemical Reagent Co. Ltd. Ag powder, Dimethyl sulfoxide-D6 (99.9%, DMSO), deuterium oxide (D_2O), and ammonia borane ($NH_3·BH_3$) was purchased from Adamas Reagent Co., Ltd. Formic acid (HCOOH) was obtained from Energy Chemical Co., Ltd. Sodium borohydride ($NaBH_4$) was acquired from Sigma-Aldrich. All chemical reagents were used directly without further purification. Ultrapure water (>18.25 MΩ cm) was used for the experiments.

1.2 Instrumentation

The powder X-ray diffraction (PXRD) patterns were recorded on an Empyrean X-ray diffractometer at 40 kV and 40 mA with Cu Kα radiation in 2θ ranging from 10^{o} to 80^{o}. Field emission scanning electron microscopy (FESEM) was performed on a Quattro S microscope operated at 5 kV. Atomic force microscopy (AFM) images were obtained on a Bruker Dimension ICON atomic force microscope. Transmission electronic microscopy (TEM) and high-resolution TEM (HRTEM) equipped with energy dispersive spectrometer (EDX) were conducted on a Talos-F200S microscope operated at 200 kV. X-ray photoelectron spectroscopy (XPS) analyses were taken on Thermo Fisher Scientific XPS ESCALAB 250Xi instrument with an Al-Ka (1486.8 eV) X-ray source. The XANES and EXAFS experiments of Ag were carried out in fluorescence mode at the BL14W1 beamline of the Shanghai Synchrotron Radiation Facility (SSRF), China. The EXAFS raw data were then background-subtracted, normalized and Fourier transformed by the standard procedures with the IFEFFIT package. Raman spectra were conducted on LabRAM HR evolution with 532 nm wavelength laser source.

1.3 Preparation

Preparation of $AgVO_3$-NB-NWs: In a typical process for preparation of $AgVO_3$-NB-NWs, 0.108 g of NH_4VO_3 was dissolved in 180 mL of water, followed by adding 180 mL of 7 mM $AgNO_3$ solutions (containing 126 mL water and 54 mLCH_3CN). After stirred for 2 h at 25 ^{o}C, the reaction mixture formed a homogeneous yellow suspension. Subsequently, they were transferred into a 500-mL stainless steel autoclave and put into furnace at 150 ^{o}C for 12 h, then cooled to room temperature naturally, and a yellow color cylindrical structure from bottom to top of the autoclave was observed. Afterwards, the product was collected by filtration, washed several times with water, and dried by vacuum freeze-drying, and yellow woven networks composed of nanobelts was obtained in one batch.

Preparation of Ag-NB-NWs: the pseudomorphic transformation of $AgVO_3$-NB-NWs to Ag-NB-NWs was performed via $NH_3{\cdot}BH_3$ as reducing agent in an ethanolic solution. First, 0.018 g of $AgVO_3$ precursor was dispersed in 10 mL of ethanol with sonication for 10 min. Subsequently, 5 mL of ethanol solution of $NH_3{\cdot}BH_3$ (0.26 M) as added to the above mixture with magnetic stirring

at 25 °C until the solution completely changed to dark brown (about 30 min). Finally, the derived Ag-NB-NWs was collected, washed, and dried at 40 °C for 12 h under vacuum.

***Preparation of Ag NPs**:* In a typical procedure, 0.085 g of $AgNO_3$ solution was dissolved in 60 mL of 0.5 M NaOH solution, followed by addition of 10 mL of 0.11 M $NaBH_4$ solution with sonication for 30 min. After stirring for 1 h, the product was collected, washed with distilled water, and dried at 40 °C for 12 h under vacuum.

1.4 Electrochemical measurements

During the CO_2 electrolysis, gaseous products were detected by an on-line gas chromatography (GC) (GC 2020) equipped with a molecular sieve 5 Å and two porapak Q columns continuously. The concentration of H_2 and CO was analyzed by a thermal conductivity detector (TCD) and a flame ionization detector (FID), respectively. The quantification of gaseous products was carried out using a conversion factor derived from the standard calibration gases. Liquid products were collected at the end of each electrocatalysis and analyzed by 1H NMR (AVANCE NEO 400). For the NMR, 0.5 mL of the catholyte was mixed with 0.1 mL of D_2O containing dimethyl sulfoxide (DMSO, 10 ppm) as the internal standard. The products concentration was quantitatively determined from its NMR peak area relative to that of the internal standard using the calibration curve from a series of standard solutions.

***Preparation of electrodes*:** Gas-diffusion electrodes were prepared by spraying catalysts onto a gas-diffusion layer (GDL) using an airbrush technique. To prepare the cathode electrode, 20 mg of catalyst, 0.95 mL of ethanol and 0.05 mL of Nafion solution were mixed to form a well-dispersed catalyst slurry, which was slowly sprayed onto a GDL to achieve a catalyst loading of ~1 mg cm^{-2}.

Flow cell measurements: Flow cell experiments were performed in a custom-designed flow cell reactor. It consisted of a gas diffusion electrode (GDE) loaded with Ag (1.0×1.0 cm^2) as the cathode, a piece of anion exchange membrane (Fumapem FAA-3-PK-130) as the separator, and a porous nickel foam as the anode. Ag/AgCl reference electrode was located inside the cathode compartment. During the measurements, CO_2 gas was directly fed to the cathodic GDE at a rate of 60 sccm. The catholyte was 1 M KOH (pH = 14). It was forced to continuously circulate through the cathode compartment at a rate of 40 mL min^{-1}. All potentials were converted to the reversible hydrogen electrode (RHE) reference scale ($E_{RHE} = E_{Ag/AgCl} + 0.198\ V + 0.0591\ V \times pH - 0.9 \times i \times$

R_{cell} V).

Membrane electrolyte assembly measurements: MEA cell was provided by Wuhan Zhisheng New Energy Co., Ltd, and experiments were operated on a 4 cm^2 self-made cell with Ti plate as flow field, consisting of a cathode, an anion exchange membrane (Nmethyl-piperidine-co-p-terphenyl, QAPPT) and an anode (IrO_2–Ti mesh). The QAPPT membrane was pre-activated in 1 M KOH at 60 ^oC for 24 h prior to usage. Two PTFE gaskets were placed in between cathodic and anodic flow plates to avoid short-circuiting. A 100 sccm humidified CO_2 was delivered through the cathodic Ti flow field in the absence of the catholyte, while the anode, 200 mL of 10 mM CsOH solution was circulated to the chamber. The CO_2RR was then initiated and the corresponding current was recorded. Potentials reported in MEA electrolyzer were non-iR corrected full-cell potentials.

CO_2RR//FOR measurements: Full cell experiments also performed in a MEA cell, 2 mg cm^{-2} Ag NBs was air-brushed onto 2 × 2 cm^2 GDL as a CO_2RR cathode and a formaldehyde oxidation reaction (FOR) anode, respectively. The CO_2 is pre-humidified before flow into the cathode plate to keep the ion exchange membrane moist. 1 M KOH with the addition of 0.1 M formaldehyde as FOR anolyte with the flow rate of 20 mL min^{-1}, anion exchange membrane (AEM) acts as solid electrolyte. Gas product of FOR is quantitatively analyzed by GC equipped with TCD and FID, and liquid product formate produced by FOR is quantitatively analyzed by 1H NMR. The concentration of formaldehyde during electrolysis was quantified via UV–vis absorption measurement following the Hantzsch reaction. Ammonium acetate (15.4 g) in water (50 mL), glacial acetic acid (0.3 mL), and acetylacetone (0.2 mL) were mixed to form a solution under stirring, which was further diluted with water (49.5 mL). To measure the concentration of formaldehyde, 20.0 μL of anolyte was acidified by 20 μL 2.0 M HCl and then diluted 2500 times prior to and post-electrolysis. Subsequently, 2.0 mL of the diluted solution was mixed with the acetylacetone solution (2.0 mL), which was further heated to 60 °C for 10 min. After cooling for 10 min, the absorbance of the sample solution at 413 nm was measured. The quantification of HCHO was obtained from the calibration curves by applying standard solutions with known concentrations of commercially purchased pure HCHO.

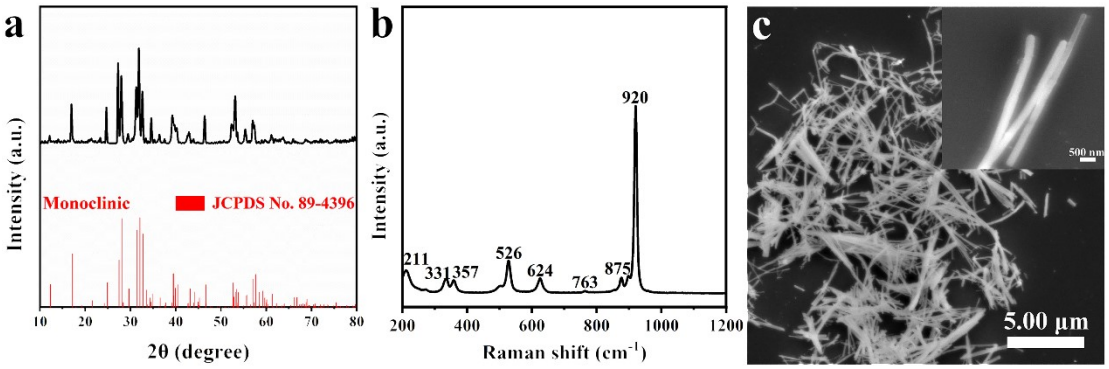

Figure S1. Characterization of $AgVO_3$ NRs: (a) XRD pattern; (b) Raman spectrum; (c) SEM image.

Diffraction peaks of the samples can be assigned to metastable α-$AgVO_3$ with monoclinic structure (ICDS No. 89-4396, space group:C2/c (No. 15)), and peaks of other phases were not detected (**Fig. S1a**). In the Raman spectra of products, the strong peaks at 920 cm^{-1} are characteristic of V–O–Ag or O–V–O stretching, whereas the peaks at 763, 624 and 526 cm^{-1} belong to V–O–V stretching vibration and the peak at 875 cm^{-1} assigns to Ag–O–Ag stretching vibrations (**Fig. S1b**). These peaks along with those located at 331, 357, and 211 cm^{-1} are the distinct signature of the $AgVO_3$ phase. SEM image of $AgVO_3$ in **Fig. S1c** shows that the samples compose of a large quantity of nanorods with the length ranging from 5 to 10 μm. High magnification SEM images show the width of the appointed nanorods about 300 nm range.

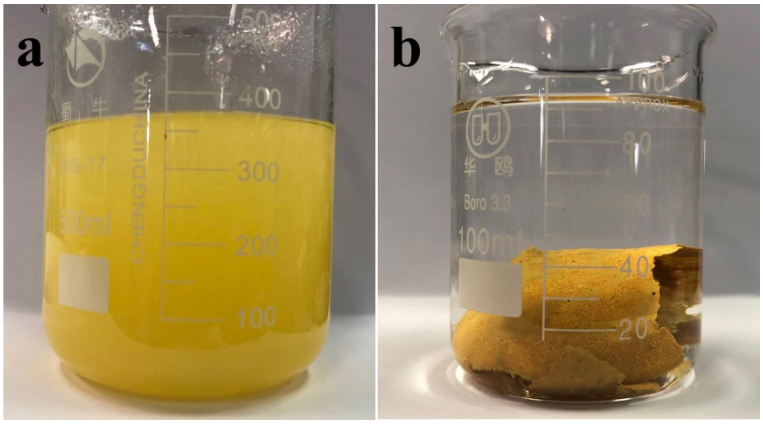

Figure S2. Optical photographs of the products before (a) and after (b) the hydrothermal treatment.

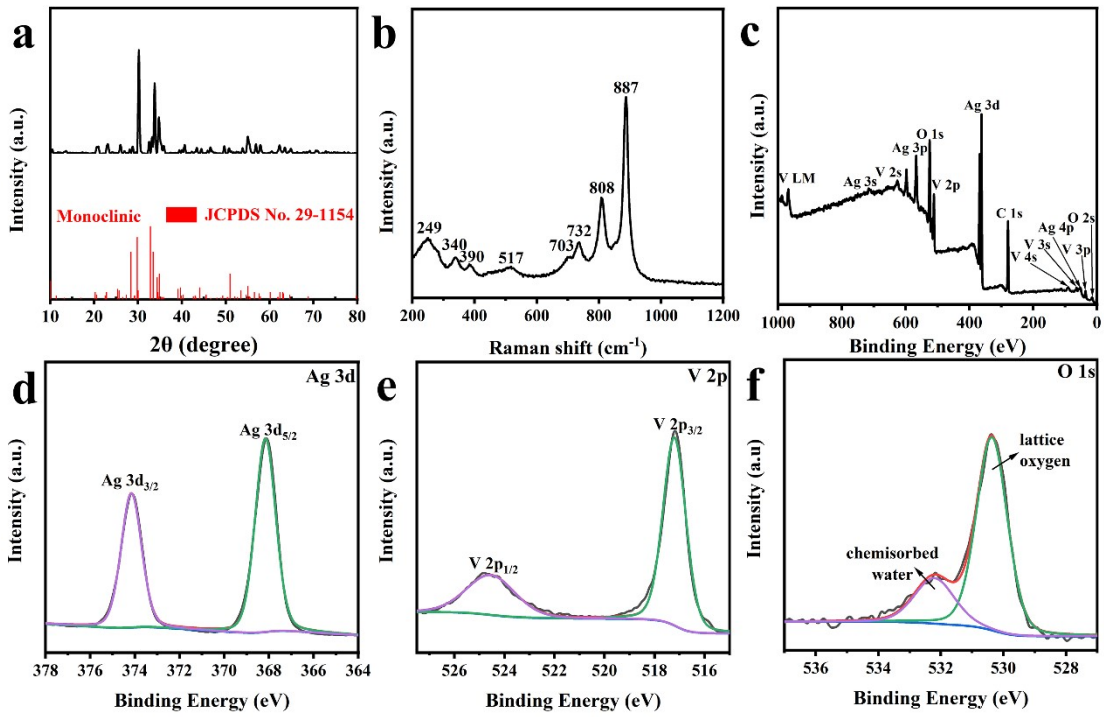

Figure S3. Characterization of $AgVO_3$-NB-NWs: (a) XRD pattern; (b) Raman spectrum; XPS spectra: (c) full spectrum; (d) Ag 3d; (e) V 5f; (f) O 1s.

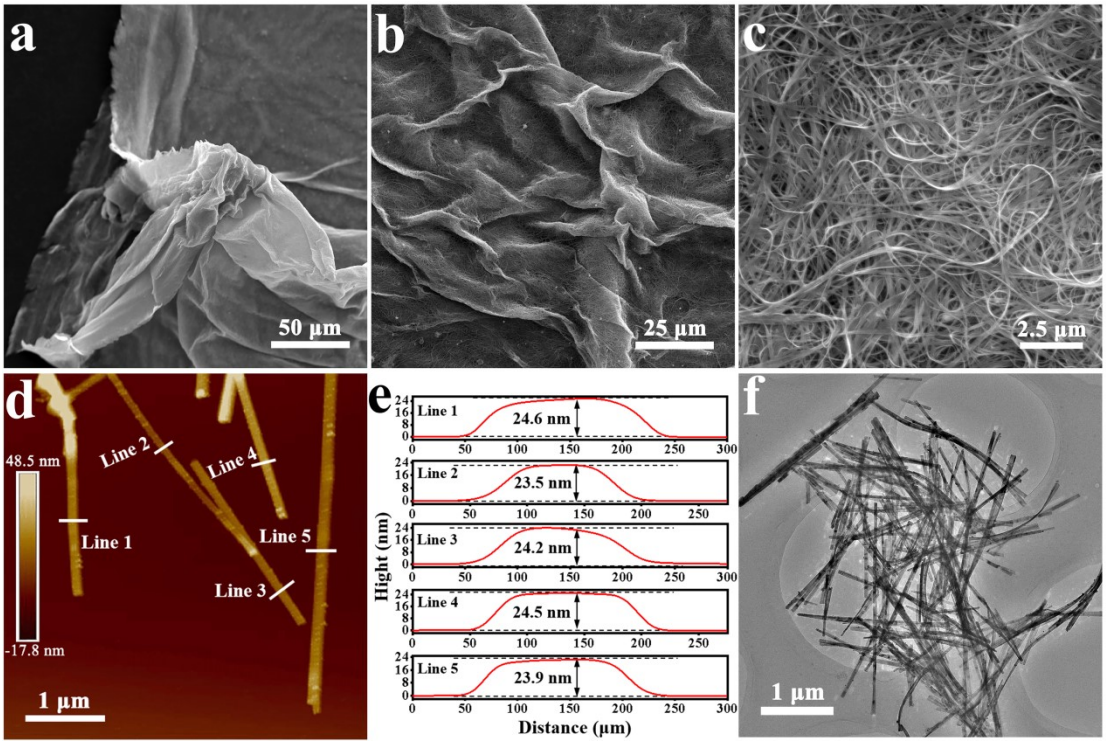

Figure S4. Characterization of $AgVO_3$-NB-NWs: (a-c) SEM images; (d, e) AFM image and corresponding height profiles; (f) TEM image.

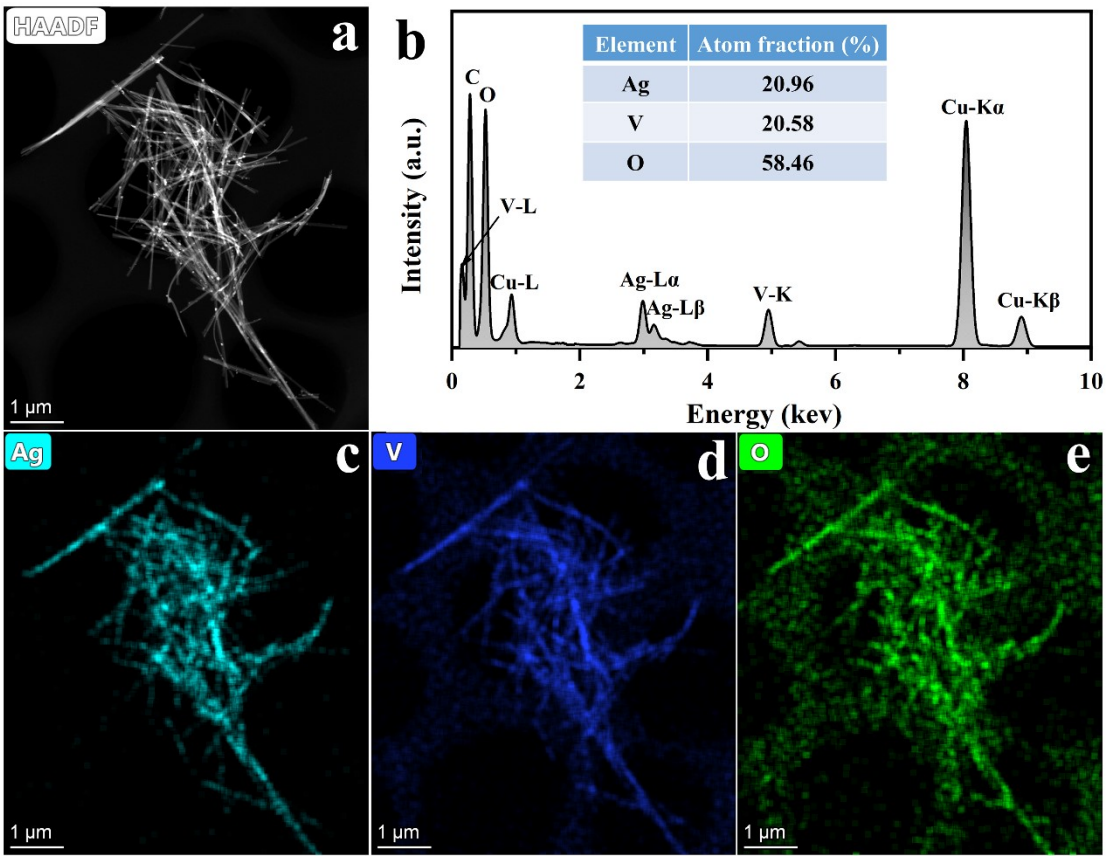

Figure S5. Characterization of $AgVO_3$-NB-NWs: (a) HAADF-STEM image; (b) EDS spectrum; EDS mapping images of (c) Ag, (d) V, and (e) O elements.

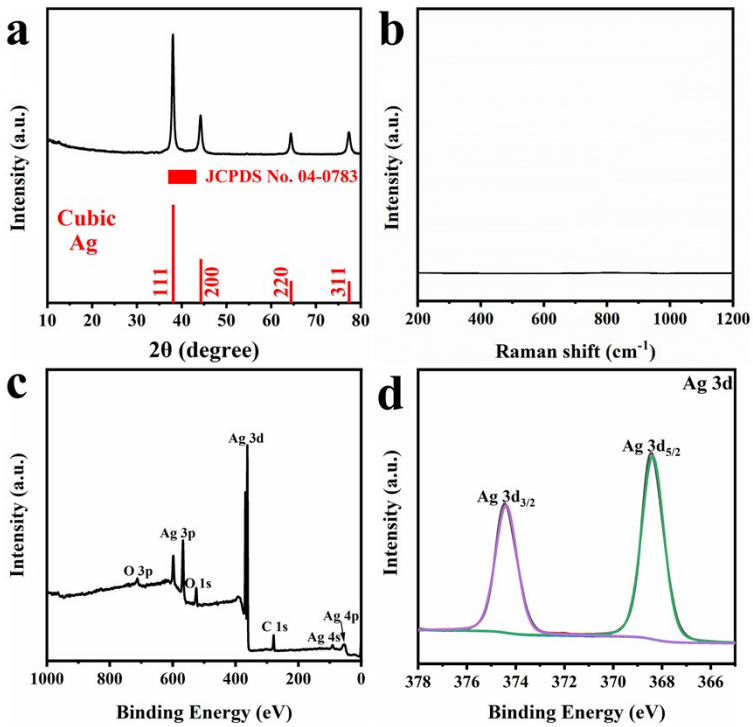

Figure S6. Characterization of Ag-NB-NWs: (a) XRD pattern; (b) Raman spectrum; XPS spectra: (c) full spectrum; (d) Ag 3d.

The O element in full spectrum originates from conductive base (**Fig. S6b**).

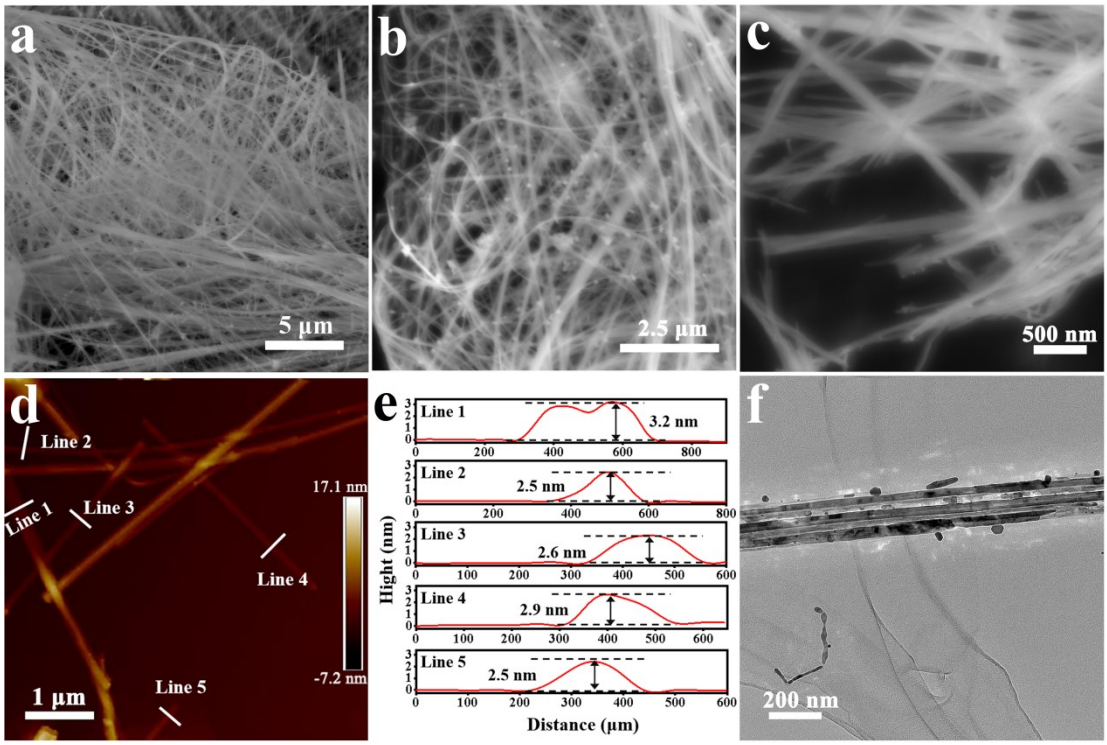

Figure S7. Characterization of Ag-NB-NWs: (a-c) SEM images; (d, e) AFM image and corresponding height profiles; (f) TEM image.

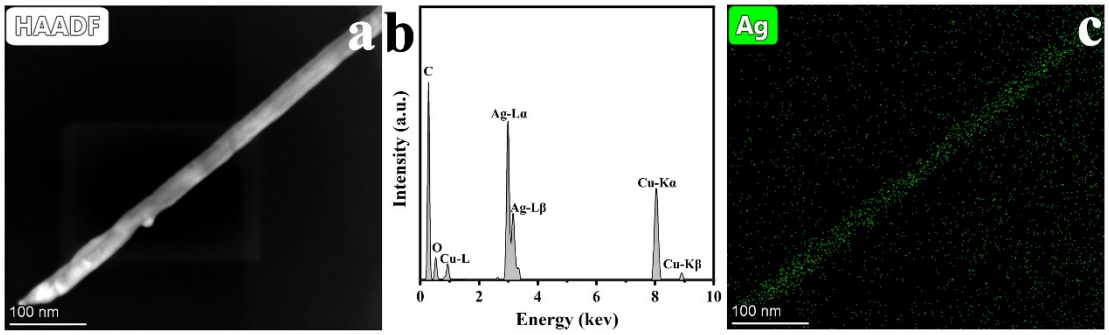

Figure S8. Characterization of Ag-ene NBs (a) HAADF-STEM image; (b) EDS spectrum; (c) EDS mapping images of Ag element.

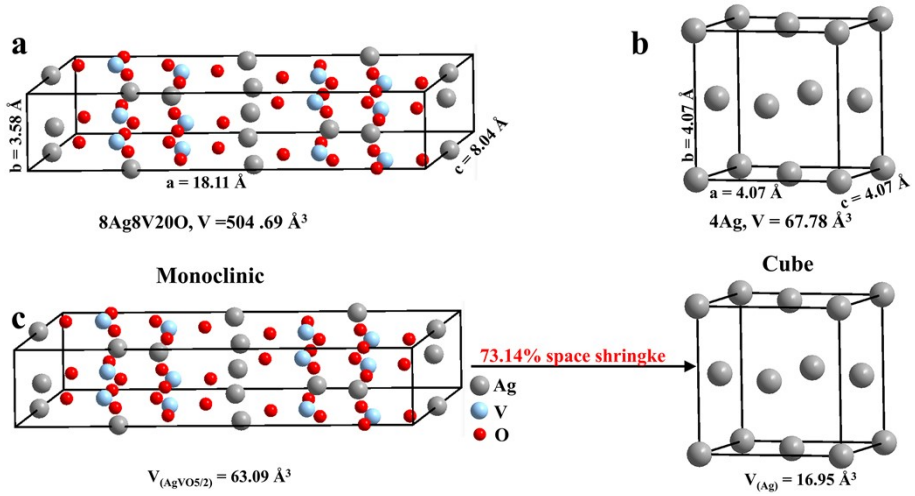

Figure S9. Theoretical investigation of the space shrinkage from monoclinic β-$AgVO_3$ to cube Ag upon the pseudomorphic transformation: (a, b) Unit cell parameters of $AgVO_3$ and Ag; (c) Volumes normalized to Ag atoms and space shrinkage upon the transformation of $AgVO_3$ to metallic Ag.

Fig. S9 shows the unit cell parameters of β-$AgVO_3$ and Ag. The cell volumes of $AgVO_3$ and Ag are 504.69 (containing 8 Ag, 8 V and 20 O atoms) and 67.78 Å^3 (containing 4 Ag atoms), respectively, where their volumes normalized to Ag atoms are calculated to be 63.09 and 16.95 Å^3, respectively. Correspondingly, the space shrinkage upon the transformation of $AgVO_3$ to metallic Ag should be 73.14%.

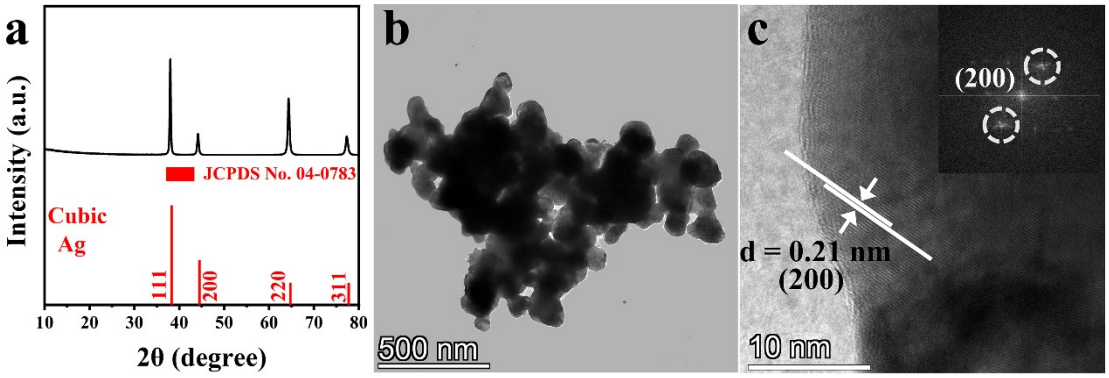

Figure S10. Characterization of Ag NPs: (a) XRD pattern; (b) TEM image; (c) HRTEM image.

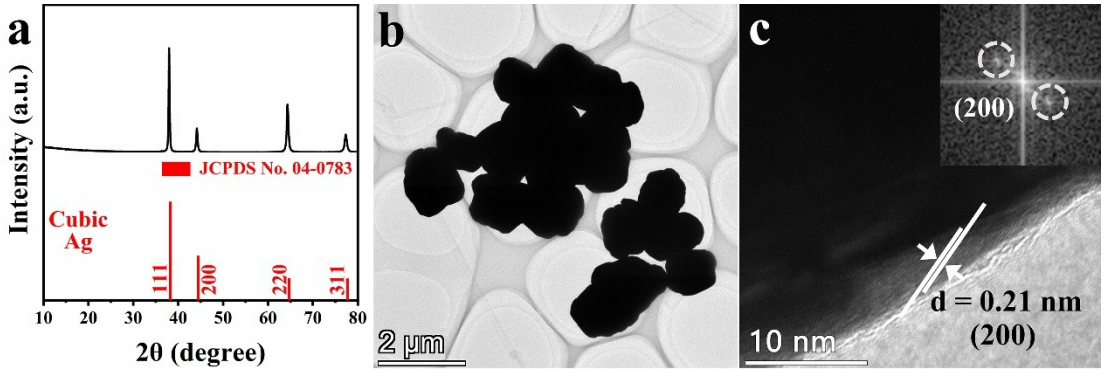

Figure S11. Characterization of Ag MPs: (a) XRD pattern; (b) TEM images; (c) HRTEM image.

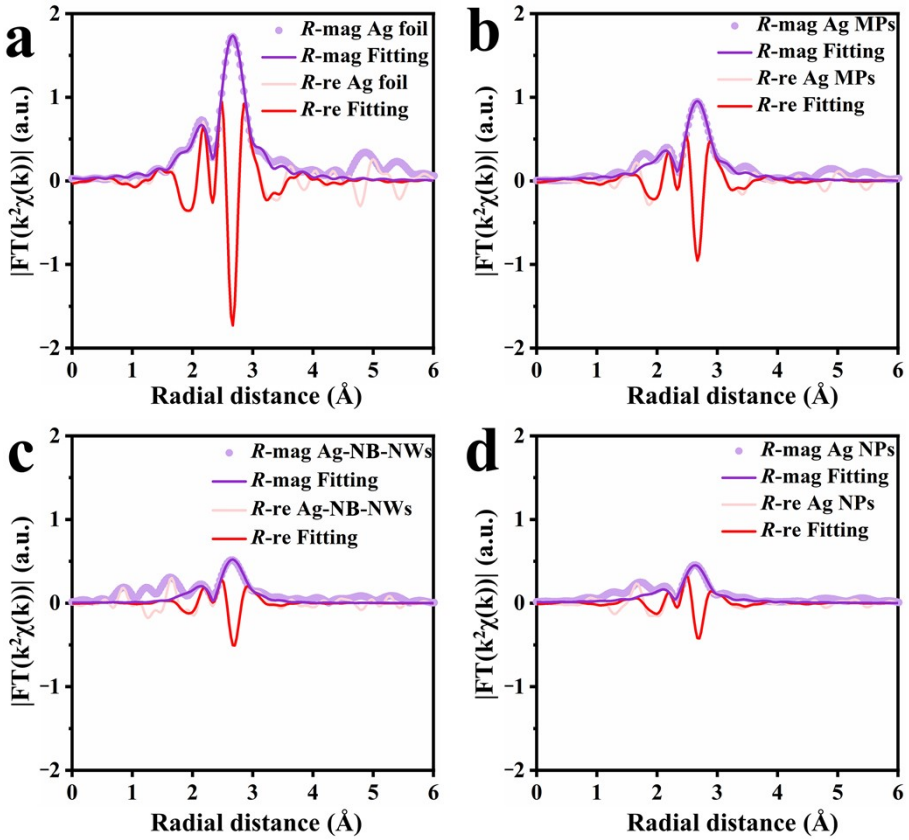

Figure S12. Experimental and fit data of Ag K-edge FT-EXAFS spectra in R space for (a) Ag foil; (b) Ag MPs; (c) Ag-NB-NWs; (d) Ag NPs.

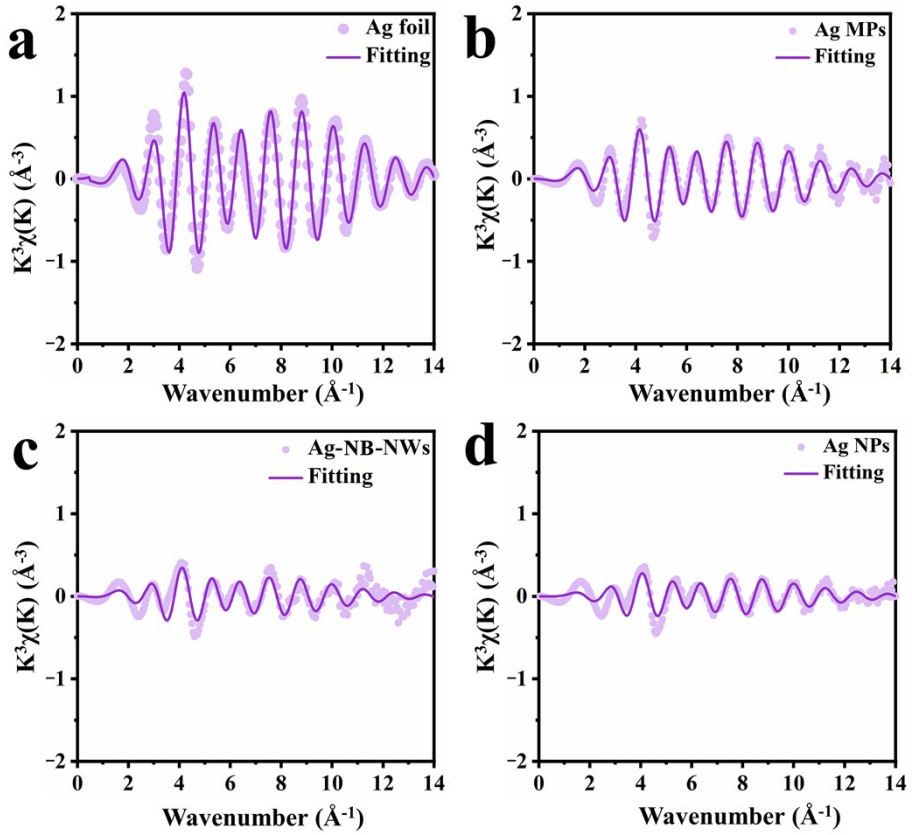

Figure S13. Experimental and fit data of Ag K-edge FT-EXAFS spectra in K space for (a) Ag foil; (b) Ag MPs; (c) Ag-NB-NWs; (d) Ag NPs.

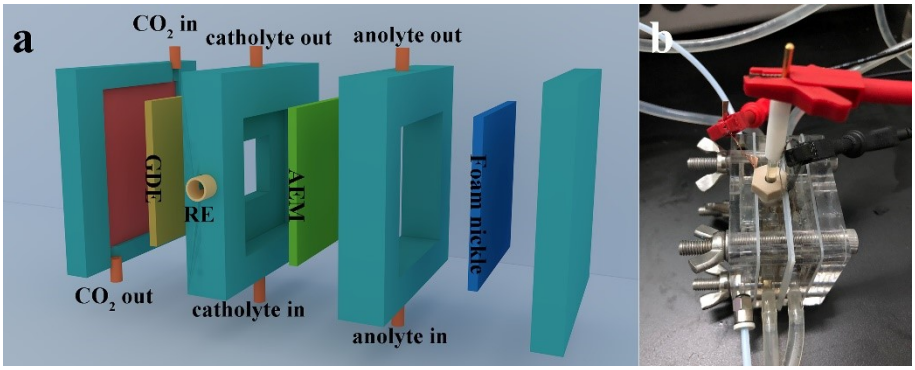

Figure S14. Flow cell configuration for electrocatalytic CO_2 reduction: (a) schematic diagram; (b) photograph of assembled reactor.

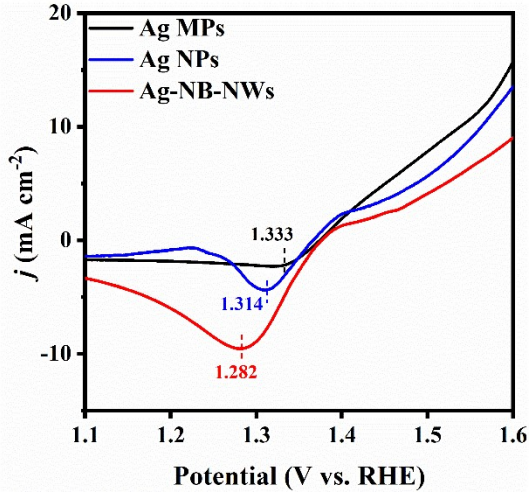

Figure S15. LSV curves of different Ag-based catalysts in Ar-saturated 0.1 M KOH electrolyte.

The overpotential of hydroxyl adsorption is considered a measure of binding strength of intermediates on catalytic surface, and the smaller overpotential indicates the larger binding energy (stronger binding) of intermediates. Due to the similar binding behaviors, the adsorption of OH^- as a surrogate of CO_2*^- was examined through a cathodic LSV scan between 1.1 and 1.6 V in Ar-saturated aqueous 0.1 M KOH solution at a scan rate of 20 mV s^{-1}.

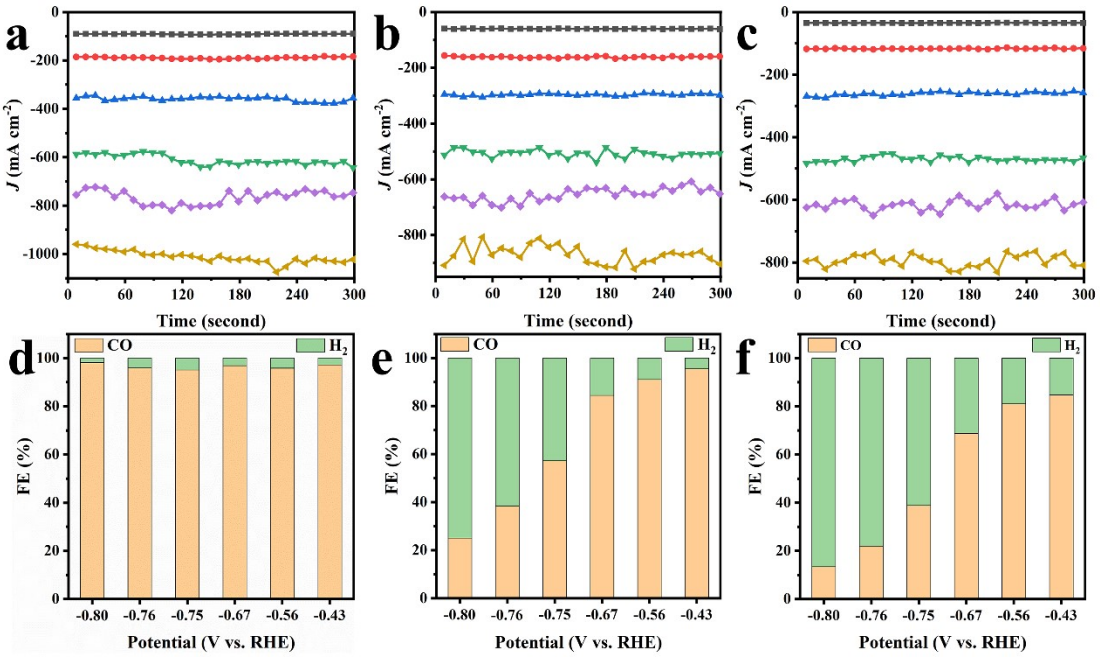

Figure S16. Electrocatalytic CO_2RR performance in flow cell using different catalysts: chronoamperometric responses at different potentials and corresponding FE for CO and H_2 on (a, d) Ag-NB-NWs; (b, e) Ag NPs; (c, f) Ag MPs.

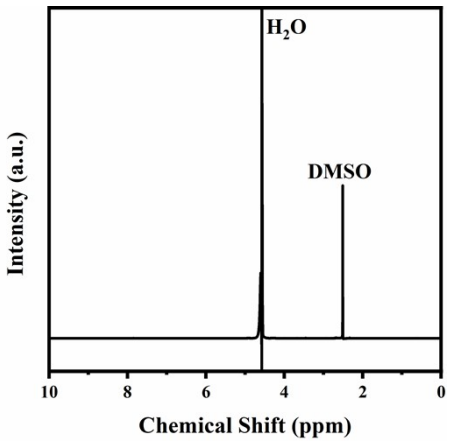

Figure S17. NMR spectroscopy in D_2O of 1 M KOH electrolyte after the electrocatalytic CO_2RR in flow cell.

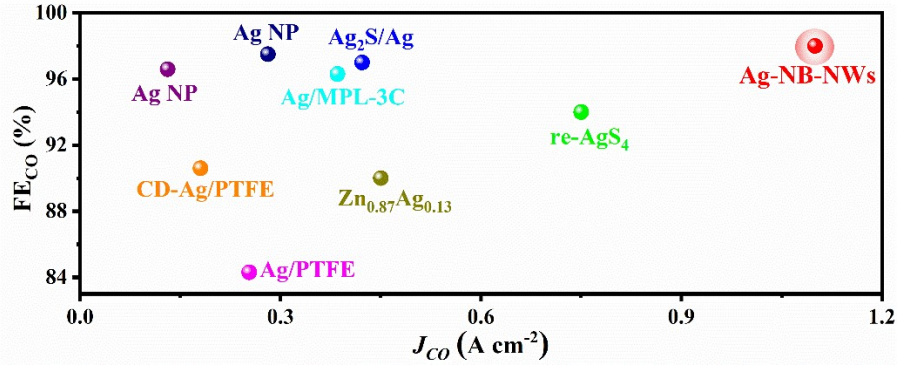

Figure S18. Comparison of the performance of Ag-NB-NWs with other Ag-based catalysts of Flow-type reactor.

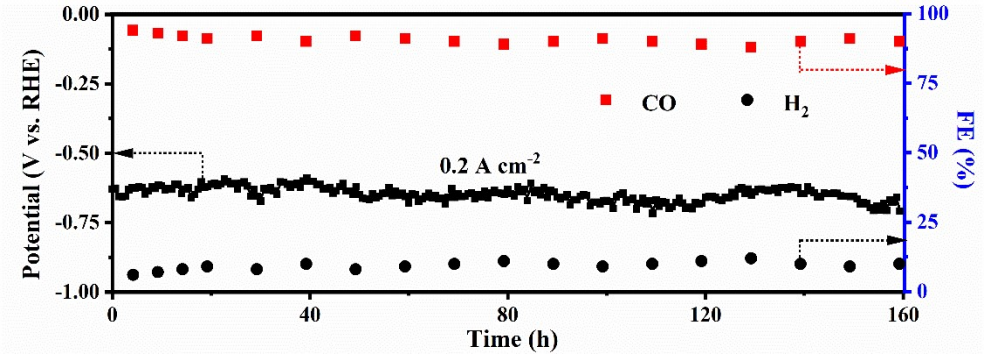

Figure S19. Long-term chronopotentiometric stability of Ag-NB-NWs in flow cell using 1 M KOH electrolytes.

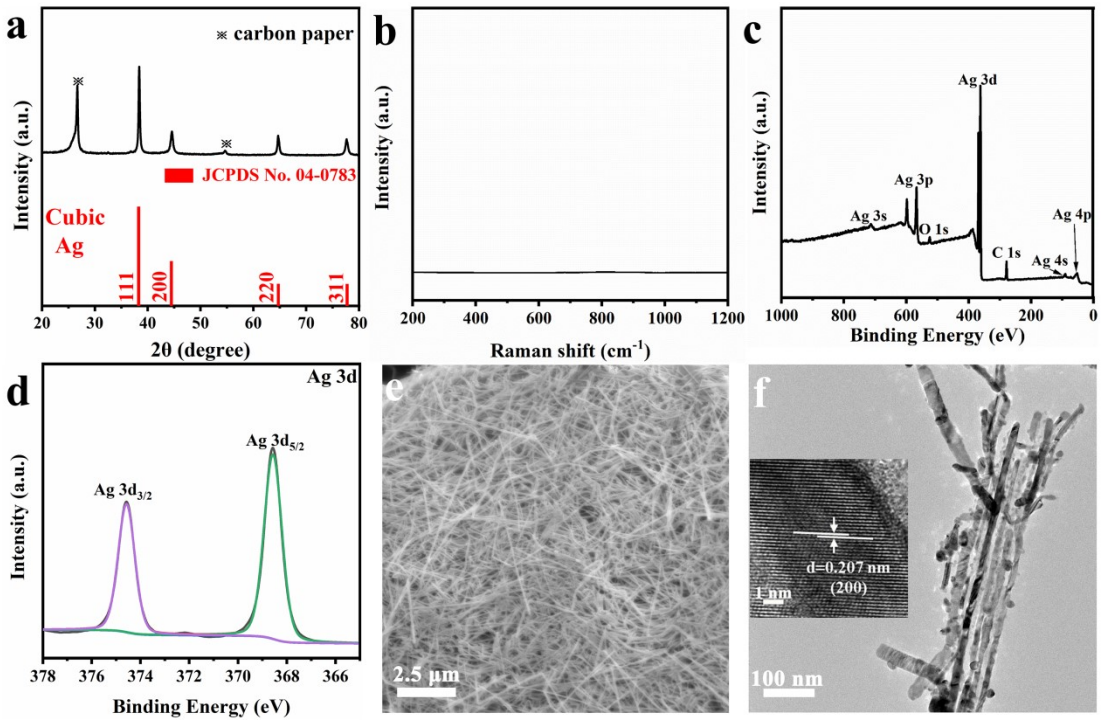

Figure S20. Characterization of $AgVO_3$-NB-NWs after long-term stability test: (a) PXRD pattern; (b) Raman spectrum; XPS spectra: (c) full spectrum; (d) Ag 3d; (e) SEM images; (f) TEM image, inserted is HRTEM image.

The crystalline state, morphology and surface condition of the recycled Ag-NB-NWs also were surveyed by PXRD, Raman, XPS, and SEM measurements. No obvious change in crystalline, composites, and state for the recycled Ag-NB-NWs was observed in **Fig. S20a-d**. SEM and TEM images in **Fig. S20e, f** show that their morphology remains the same before and after the electrolysis. The O element in full spectrum originates from conductive base (**Fig. S20c**).

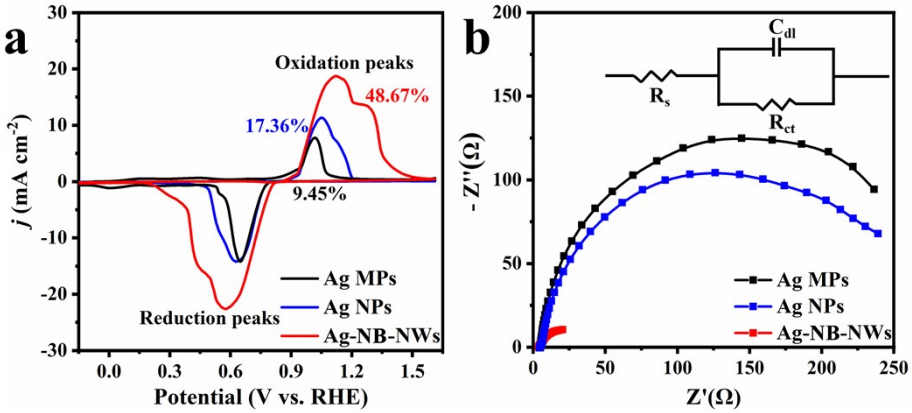

Figure S21. Different Ag-based catalysts for electrocatalytic CO_2 reduction: (a) CV curves; (b) Nyquist plots (Inset is the equivalent circuit consisting of an ohmic resistance of the electrolyte ($_{Rs}$), a charge transfer resistance between catalyst and electrolyte (R_{ct}) and a constant phase element (C_{dl})).

CV curves of Ag-NB-NWs, Ag NPs and Ag MPs electrode in a potential range from −0.1 to 1.57 V are shown in Fig. S21a at a scan rate of 100 mV s^{-1}. The oxidation peak at 1.17 V over Ag-NB-NWs belongs to the conversion of metallic Ag to Ag^+, the reduction peak at 0.56 V belongs to the conversion of Ag^+ to metallic Ag.

Based on the oxidation peak, the percentage (χ) of active Ag sites to the total Ag sites can be calculated as follows:

$$\chi = S_{op} / (n_{total} \times N \times v \times F \times S_{area}) \times 100\%$$

where S_{op} is area of oxidation peak, n_{total} is the total Ag sites which refers to the molar amount of Ag based on Ag_2O loaded to the electrode, N is the number of electrons required to convert Ag to Ag^+, v is scan rate, F is Faraday constant (96485 C mol^{-1}), S_{area} is the area of electrode.

The electrochemical impedance spectroscopy (EIS) was recorded at –0.1 V vs. RHE with the frequency ranging from 0.1 to 10^5 Hz at the AC amplitude of 5 mV (Fig. S21b).

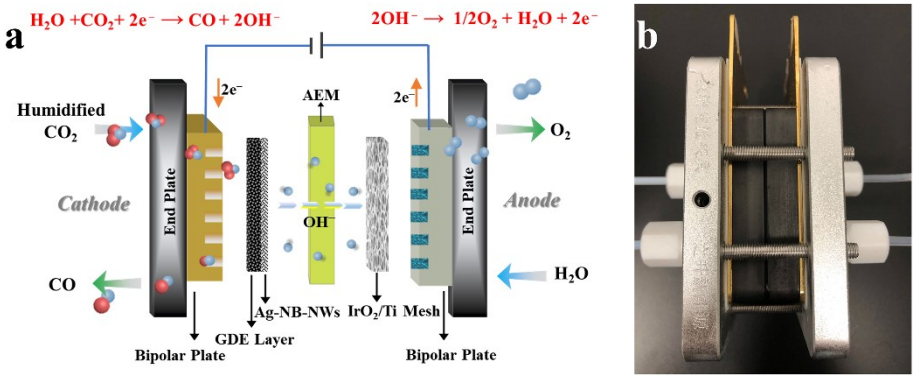

Figure S22. MEA cell configuration for electrocatalytic CO_2 reduction: (a) schematic diagram and working principle; (b) photograph of assembled reactor.

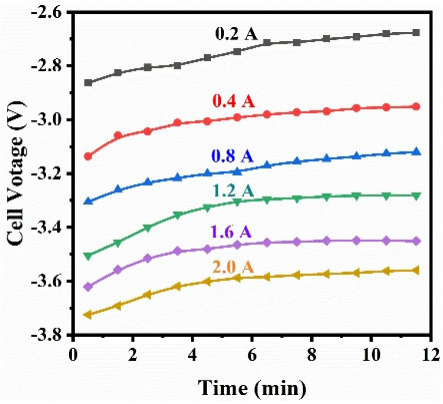

Figure S23. Chronopotentiometric responses at different currents in MEA cell.

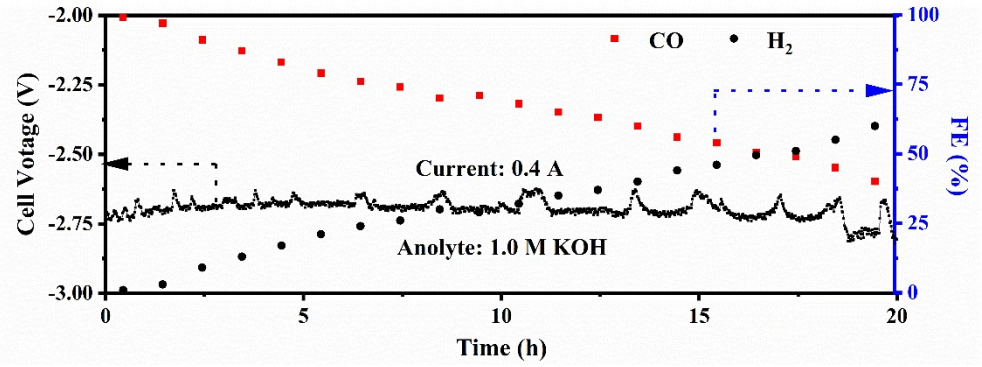

Figure S24. Stability of continuously operated Ag-NB-NWs at 0.4 A in MEA cell using 1 M KOH as anolyte: (a) chronopotentiometric curves and corresponding product selectivity; (b) photograph of salt precipitate in gas flow channel.

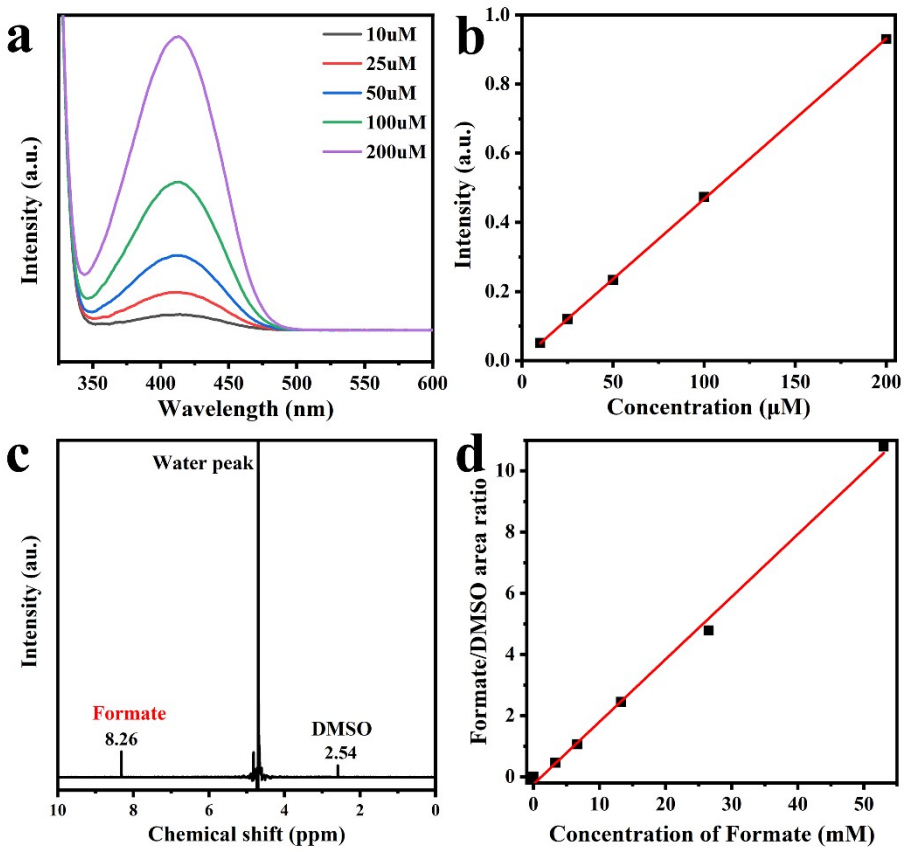

Figure S25. Identification and quantification of HCHO by UV-vis absorption spectra: (a) A typical UV-vis absorption spectra of the product from the reaction between acetyl acetone and HCHO of different known concentrations, (b) Calibration curve obtained by plotting the HCHO concentration against absorption peak intensity at λ = 413 nm; Identification and quantification of formate by NMR: (c) A typical NMR spectrum of the recycled electrolyte containing formate after electrolysis; (d) Standard curve by plotting the formate concentration with respect to the NMR peak area ratio of formate/DMSO.

Table S1. Ag K-edge EXAFS fitting results for Ag-NB-NWs, Ag NPs, Ag MPs, Ag foil, and Ag_2O.

sample	shell	N	σ^2 (Å^2)	ΔE_0 (eV)	R (Å)	R-factor
Ag foil	Ag-Ag	12(fixed)	9.6±0.2	2.0±0.2	2.86±0.00	0.002
Ag_2O	Ag-O Ag-Ag	3.8±0.2 10.9±0.5	5.6±1.2 5.6±1.2	2.1±2.4 2.1±2.4	2.04±0.03 3.34±0.01	0.017
Ag MPs	Ag-Ag	7.2±0.8	4.6±0.8	10.2±1.1	2.86±0.01	0.009
Ag-NB-NWs	Ag-Ag	4.5±0.8	11.9±1.0	-1.1±1.1	2.87±0.01	0.020
Ag NPs	Ag-Ag	3.5±0.7	10.5±1.7	-3.3±0.7	2.86±0.01	0.019

Data ranges: 3.0≤k≤ 12.4 Å^{-1}, 1≤R ≤3 Å. N: Coordination numbers; σ: Debye-Waller parameters, R: coordination distances; R-factor: goodness of fit, ΔE_0 energy shift. S_0^2 is amplitude reduction factor (S_0^2=0.83 was obtained by Ag foil fitting and applied for other sample fitting).

Table S2. Comparison of the catalytic performances of Ag-based electrocatalysts for CO_2RR to CO production in Flow-type reactor.

Catalyst	Electrolyte	Potential (V *vs.* RHE)	j_{CO} (mA cm^{-2})	FE_{CO} (%)	Stability	Reference
Ag-NB-NWs	1 M KOH	–1.0	1100	98	160 h; 200 mA cm^{-2}	This work
re-AgS_4	1 M KOH	–0.56	750	94	52 h; 30 mA cm^{-2}	S1
Ag_2S/Ag	1 M KOH	–0.70	422	97	50 h; 245 mA cm^{-2}	S2
Ag/MPL-3C	1 M KOH	−1.02	385.2	96.3	4 h; 300 mA cm^{-2}	S3
Ag/PTFE	1 M KOH	–0.84	253	84.30	100 h; 100 mA cm^{-2}	S4
CD-Ag/PTFE	1 M KOH	–0.8	180	90.6	100 h; 150 mA cm^{-2}	S5
$Zn_{0.87}Ag_{0.13}$	1 M KCl	–1.27	450	90	\	S6
Ag NP	1 M KOH	–1.21	281	97.5	\	S7
Ag NP	1 M KOH	−0.59	131	96.6	\	S8

Table S3. Comparison of the catalytic performances of Ag-based electrocatalysts for CO_2RR to CO in the MEA.

Catalyst	Anolyte	Voltage (V)	j (mA cm^{-2})	FE_{CO} (%)	EE (%)	Stability	Reference
Ag-NB-NWs	0.01 M CsOH	3.6	500	98	\	240 h; 100 mA cm^{-2}; ≥90%	This work
Ag	0.01 M CsOH	4.0	876	76	\	50 h; 500 mA cm^{-2}; ≥80%	S9
$AuAg_{12}Au_{12}$	1.0 M KOH	2.66	339	\	\	24 h; 200 mA cm^{-2}; ≥80%	S10
e-Ag coral	1 M KOH	3.5	350	90	\	30 h; 100 mA cm^{-2}; ≥70%	S11
$Zn_{0.87}Ag_{0.13}$	0.1 M Cs_2CO_3	\	400	93	32	40 h; 200 mA cm^{-2}; ≥70% 100 h; 100 mA cm^{-2}; ≥80%	S6
Ag NP	0.1 M $KHCO_3$	4.2	430	77.4	\	12 h; 160 mA cm^{-2}; ≥90%	S12
Ag NP	1 M KOH	3	300	95	\	8 h; 200 mA cm^{-2}; ≥65%	S13
Ag NP	0.1 M $KHCO_3$	3	200	94	\	\	S14
Ag NP	0.01 M H_2SO_4 0.01M Cs_2SO_4	4.0	80	40	\	50 h; 60 mA cm^{-2}; ≥30%	S15

Table S4. A comparison of electrolysis performance of inorganic and organic feedstocks electrooxidation integrated with CO_2RR in two-electrodes electrolyzer.

Paired electrolysis	Cathode			Anode			J_{total} (A)	Stability (h; A; V)	Reference
	catalyst	electrolyte	FE(%)	catalyst	electrolyte	FE (%)			
CO_2RR//FOR	Ag-NB-NWs	\	CO 98	Ag-NB-NWs	1 M KOH+ 0.1 M HCOH	HCOOH 90	1.0	200 h; 1A; 0.6 V	This work
CO_2RR//MOR	$mSnO_2$	1 M $KHCO_3$	HCOOH 80.5	CuONS	1 M KOH+ 1 M CH_3OH	HCOOH 93	0.325	\	S16
CO_2RR//MOR	Zn/SnO_2	2.0 M K_2CO_3	HCOOH 92.2	Zn/SnO_2	2.0 M K_2CO_3	H_2O_2 80.6	0.32	60 h; 0.15 A; V	S17
CO_2RR//MOR	Bi-ene	0.5 M $KHCO_3$	HCOOH 100	Ni-NF	1 M KOH+ 1 M CH_3OH	HCOOH 100	0.027	\	S18
CO_2RR//MOR	CuSn-4	0.5 M $KHCO_3$	HCOOH 90.6	CuSn-4	1 M KOH+ 1 M CH_3OH	HCOOH 96.5	0.14	\	S19
CO_2RR//MOR	Cu_2O	1 M KOH	HCOOH 78	Cu_2O	1 M KOH+ 1 M CH_3OH	HCOOH 80	0.15	\	S20
CO_2RR//PET	SnO_2	1 M $NaHCO_3$	HCOOH 80	$NiCo_2O_4$	1 M NaOH+ 0.1 M PET	HCOOH 90	0.15	\	S21
CO_2RR//GOR	NiSAs/FN-CNSs	2 M $KHCO_3$	CO >90	$CoSe_2$	2 M KOH+ 2 M glycerol	HCOOH ~90	0.3	400 h; 0.15 A; V	S22
CO_2RR//GER	N_3NiPc	0.5 M $KHCO_3$	CO ~100	N_3NiPc	0.5 M $KHCO_3$+ 1 mM L-DOPA	\	0.025	\	S23
CO_2RR//SOR	$(NH_x)_{16}$-NiPc	1 M KOH	CO ~100	$(NH_x)_{16}$-NiPc	1 M KOH+ 1.0 M Na_2S	\	0.3	\	S24

Reference

[1] J. Chen, X. Liu, S. Xi, T. Zhang, Z. Liu, J. Chen, L. Shen, S. Kawi, L. Wang, Functionalized Ag with Thiol Ligand to Promote Effective CO_2 Electroreduction, ACS Nano, 2022, 16, 13982-13991.

[2] K. Ye, T. Liu, Y. Song, Q. Wang, G. Wang, Tailoring the interactions of heterogeneous Ag_2S/Ag interface for efficient CO_2 electroreduction, Appl. Catal. B: Environ., 2021, 296, 120342.

[3] R. Wang, H. Haspel, A. Pustovarenko, A. Dikhtiarenko, A. Russkikh, G. Shterk, D. Osadchii, S. Ould-Chikh, M. Ma, W.A. Smith, K. Takanabe, F. Kapteijn, J. Gascon, Maximizing Ag Utilization in High-Rate CO_2 Electrochemical Reduction with a Coordination Polymer-Mediated Gas Diffusion Electrode, ACS Energy Lett., 2019, 4, 2024-2031.

[4] C.M. Gabardo, A. Seifitokaldani, J.P. Edwards, C.-T. Dinh, T. Burdyny, M.G. Kibria, C.P. O'Brien, E.H. Sargent, D. Sinton, Combined high alkalinity and pressurization enable efficient CO_2 electroreduction to CO, Energy Environ. Sci., 2018, 11, 2531-2539.

[5] C.-T. Dinh, F.P. García de Arquer, D. Sinton, E.H. Sargent, High Rate, Selective, and Stable Electroreduction of CO_2 to CO in Basic and Neutral Media, ACS Energy Lett., 2018, 3, 2835-2840.

[6] S. Lamaison, D. Wakerley, F. Kracke, T. Moore, L. Zhou, D.U. Lee, L. Wang, M.A. Hubert, J.E. Aviles Acosta, J.M. Gregoire, E.B. Duoss, S. Baker, V.A. Beck, A.M. Spormann, M. Fontecave, C. Hahn, T.F. Jaramillo, Designing a Zn-Ag Catalyst Matrix and Electrolyzer System for CO_2 Conversion to CO and Beyond, Adv. Mater., 2022, 34, e2103963.

[7] B. Kim, F. Hillman, M. Ariyoshi, S. Fujikawa, P.J.A. Kenis, Effects of composition of the micro porous layer and the substrate on performance in the electrochemical reduction of CO_2 to CO, J. Power Sources, 2016, 312, 192-198.

[8] S. Ma, R. Luo, J.I. Gold, A.Z. Yu, B. Kim, P.J.A. Kenis, Carbon nanotube containing Ag catalyst layers for efficient and selective reduction of carbon dioxide, J. Mater. Chem. A, 2016, 4, 8573-8578.

[9] K. Ye, G. Zhang, X.-Y. Ma, C. Deng, X. Huang, C. Yuan, G. Meng, W.-B. Cai, K. Jiang, Resolving local reaction environment toward an optimized CO_2-to-CO conversion performance, Energy Environ. Sci., 2022, 15, 749-759.

[10] H. Seong, M. Choi, S. Park, H.-w. Kim, J. Kim, W. Kim, J.S. Yoo, D. Lee, Promoting CO_2-to-CO Electroreduction via the Active-Site Engineering of Atomically Precise Silver Nanoclusters, ACS Energy Lett., 2022, 7, 4177-4184.

[11] W.H. Lee, Y.-J. Ko, Y. Choi, S.Y. Lee, C.H. Choi, Y.J. Hwang, B.K. Min, P. Strasser, H.-S. Oh, Highly selective and scalable CO_2 to CO - Electrolysis using coral-nanostructured Ag catalysts in zero-gap configuration, Nano Energy, 2020, 76, 105030.

[12] Y. Xu, J.P. Edwards, S. Liu, R.K. Miao, J.E. Huang, C.M. Gabardo, C.P. O'Brien, J. Li, E.H. Sargent, D. Sinton, Self-Cleaning CO_2 Reduction Systems: Unsteady Electrochemical Forcing Enables Stability, ACS Energy Lett., 2021, 6, 809-815.

[13] B. Endrodi, E. Kecsenovity, A. Samu, F. Darvas, R.V. Jones, V. Torok, A. Danyi, C. Janaky, Multilayer Electrolyzer Stack Converts Carbon Dioxide to Gas Products at High Pressure with High Efficiency, ACS Energy Lett., 2019, 4, 1770-1777.

[14] D. Kim, W. Choi, H.W. Lee, S.Y. Lee, Y. Choi, D.K. Lee, W. Kim, J. Na, U. Lee, Y.J. Hwang, D.H. Won, Electrocatalytic Reduction of Low Concentrations of CO_2 Gas in a Membrane Electrode Assembly Electrolyzer, ACS Energy Lett., 2021, 6, 3488-3495.

[15] B. Pan, J. Fan, J. Zhang, Y. Luo, C. Shen, C. Wang, Y. Wang, Y. Li, Close to 90% Single-Pass Conversion Efficiency for CO_2 Electroreduction in an Acid-Fed Membrane Electrode Assembly, ACS Energy Lett., 2022, 7, 4224-4231.
[16] X. Wei, Y. Li, L. Chen, J. Shi, Formic Acid Electro-Synthesis by Concurrent Cathodic CO_2 Reduction and Anodic CH_3OH Oxidation, Angew. Chem. Int. Ed., 2021, 60, 3148-3155.
[17] C. Cao, D.D. Ma, J. Jia, Q. Xu, X.T. Wu, Q.L. Zhu, Divergent Paths, Same Goal: A Pair-Electrosynthesis Tactic for Cost-Efficient and Exclusive Formate Production by Metal-Organic-Framework-Derived 2D Electrocatalysts, Adv. Mater., 2021, 33, e2008631.
[18] Y. Li, C.-Z. Huo, H.-J. Wang, Z.-X. Ye, P.-P. Luo, X.-X. Cao, T.-B. Lu, Coupling CO_2 reduction with CH_3OH oxidation for efficient electrosynthesis of formate on hierarchical bifunctional CuSn alloy, Nano Energy, 2022, 98, 107277.
[19] D. Tan, B. Wulan, J. Ma, X. Cao, J. Zhang, Interface Molecular Functionalization of Cu_2O for Synchronous Electrocatalytic Generation of Formate, Nano Lett., 2022, 22, 6298-6305.
[20] A. Vass, A. Kormanyos, Z. Koszo, B. Endrodi, C. Janaky, Anode Catalysts in CO_2 Electrolysis: Challenges and Untapped Opportunities, ACS Catal., 2022, 12, 1037-1051.
[21] G. Wang, J. Chen, K. Li, J. Huang, Y. Huang, Y. Liu, X. Hu, B. Zhao, L. Yi, T.W. Jones, Z. Wen, Cost-effective and durable electrocatalysts for Co-electrolysis of CO_2 conversion and glycerol upgrading, Nano Energy, 2022, 92, 106751.
[22] D.-D. Ma, S.-G. Han, C. Cao, W. Wei, X. Li, B. Chen, X.-T. Wu, Q.-L. Zhu, Bifunctional single-molecular heterojunction enables completely selective CO_2-to-CO conversion integrated with oxidative 3D nano-polymerization, Energy Environ Sci., 2021, 14, 1544-1552.
[23] S.G. Han, M. Zhang, Z.H. Fu, L. Zheng, D.D. Ma, X.T. Wu, Q.L. Zhu, Enzyme-Inspired Microenvironment Engineering of a Single-Molecular Heterojunction for Promoting Concerted Electrochemical CO_2 Reduction, Adv. Mater., 2022, 34, e2202830.